JACS
JOURNAL OF THE AMERICAN CHEMICAL SOCIETY
pubs.acs.org/JACS
Article

Electrodepositing Textured Sn Film as a Highly Reversible Anode for Aqueous Batteries

Haozhe Zhang, Yanxia Yu, Diyu Xu, Minghao Zhang, Chen-Jui Huang, Jianxin Wang, Hao Liu, Fan Yang, Mingqian Li, Di-Jia Liu, Xihong Lu,* Kang Xu,* and Ying Shirley Meng*

Cite This: https://doi.org/10.1021/jacs.5c03861

Read Online

ACCESS | Metrics & More | Article Recommendations | Supporting Information

ABSTRACT: Electrodepositing metal materials in large capacity, at low potential, and with high reversibility serves as the foundation for any aqueous rechargeable battery chemistry to realize the promises of high energy, low cost, and high safety. However, such a foundation is not solid because of the natural tendency of metals to form irregular, nonplanar, and often dendritic morphologies during electrochemical crystallization, which is further amplified in an acidic environment due to the faster kinetics of the coupled proton and mass-transport processes between hydrated metal ions and free metal atoms. As a typical representative, tin metal (Sn^0) has potential to achieve high energy in acidic batteries, but its nonuniform large-particle morphology, obtained from traditional electrodeposition, leads to dead Sn^0 formation and deteriorating reversibility, accompanied by the sustained hydrogen evolution reaction (HER) and active Sn^0 loss. Here, we report quaternary onium salts as effective interfacial cocations that, via selective adsorption, steadily texturize Sn^0 deposition along the (211) plane, which is intrinsically inert to the HER, thus regulating the film deposition process by favoring the formation of planar Sn^0 film. Such Sn^0 film brings exceptional reversibility in acidic electrolytes, which translates into sustained cycling stability at applicable areal capacities in both anode-half cells (~1500 deposition/dissolution cycles at 5 mAh cm^{-2}) and full cells (350 charge/discharge cycles at 5 mAh cm^{-2}). Textured electrodeposition with intrinsic HER-suppression capability provides a universal solution for diverse metal anode materials in rechargeable energy-dense aqueous batteries.

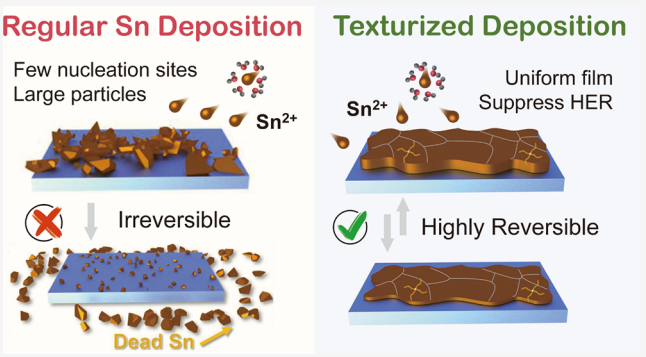

1. INTRODUCTION

The increasing need for reliable and cost-effective battery technologies calls for the development of systems capable of supporting large-scale energy storage and broad adoption in daily residential and industrial applications.[1,2] Aqueous batteries offer unique advantages in safety and cost in comparison with other diverse battery chemistries like the prevailing Li-ion batteries, due to the utilization of cheap and incombustible water-based electrolytes that are no longer heavily reliant on an anhydrous, oxygen-free fabrication environment or strict battery management systems.[3,4] Similar to their nonaqueous counterparts using Li, Na, and Mg anodes, aqueous batteries also widely leverage the electrodeposition of metals from electrolytes in order to maximize the output voltage, capacity, and overall energy density.[5,6] Acidic batteries especially benefit from electrodeposited metals to match existing cathodes of high energy and high kinetics.[7−10] However, the reversibility of metal electrodeposition/dissolution remains a universal challenge, even in the most well-established battery systems. Porous, nonplanar, and often dendritic morphologies of metals generated by repeated uncontrolled deposition processes lead to severe side reactions, resulting in low Coulombic efficiency (CE), incessant consumption of electrolytes and electrode active materials, and even short-circuiting of the batteries.[11] The scenario becomes even more challenging in an acidic environment, where the high proton activity drives severe corrosion of active metals and promotes the hydrogen evolution reaction (HER). In addition, the stronger hydrogen bonding network in the acidic electrolytes reduces the desolvation energy of hydrated metal ions, leading to faster transformation between metal ions and metal atoms, as characterized by higher exchange current densities (j_0) and lower overpotential (η).[12] The combined effect of these factors makes the nucleation process more difficult, with the formation of scattered large particles favored during the uncontrolled metal electrodeposition.[13,14]

Received: March 4, 2025
Revised: May 13, 2025
Accepted: May 14, 2025

Ideal electrodeposition of metals in a rechargeable battery should result in a homogeneous and polycrystalline dense film with high conformity (Figure S1).[15] Flat film morphology not only minimizes the surface area for side reactions such as the HER but also circumvents mechanical damage to the separator or membrane that could create a short-circuit. Furthermore, since only the top side of the film is exposed to the electrolyte, particle detachment from the current collector can also be effectively suppressed. In contrast, a nonplanar metal surface with large particles or even dendrite morphology often becomes the growth "hotspot", magnifying the height differences among various electrodeposition sites, mechanically damaging the separator, and encouraging side reactions.[16] More often than not, during dissolution, the bottom section of the deposited particle exposed to the electrolyte would preferentially oxidize and dissolve due to the shorter pathway for electron transport, hence triggering the formation of "dead" metal particles that are electrically detached from the underlying current collector.[17] Therefore, controlling the growth of electrodeposited metal into a film morphology constitutes the foundation for practical applications of rechargeable metal batteries with high reversibility.

Metal electrodeposition consists of multiple-step processes that include the transport of solvated metal ions to the electrolyte/electrode interface, their desolvation and reduction by incoming electrons, adsorption of free metal atoms on electrodes, and subsequent diffusion along the lattice planes of either homo- or heteromaterials, ultimately forming a new layer as governed by the lattice structure to complete particle growth.[18] During electrodeposition, the nascent metal atom may expose not only one, but most likely several lattice planes, with varying texture and morphology being characteristic of different metals and codetermined by total energy changes during deposition—namely, changes in surface, strain, and thermal energy.[19−21] The surface energy of a specific lattice plane is the energy required to create a unit area of that surface. Strain energy is influenced by intrinsic factors, such as atomic mobility, and extrinsic factors, such as applied stacking pressure. Moreover, grains exhibiting high thermal conductivity are preferred because they promote efficient dissipation of heat during the deposition process. Since thermal anisotropy is typically negligible in thin films, surface energy (thermodynamic factor) and self-diffusion barrier (kinetic factor) become the primary competing influences on grain orientation to minimize the total energy under conditions without additional stacking pressure. From a thermodynamic aspect, the Gibbs−Curie−Wulff theory posits that an equilibrium shape with a specific combination of lattice planes that minimizes the surface energy is preferred during ideal crystal growth.[22] Meanwhile, a low self-diffusion barrier indicates that the deposited metal atom has high mobility within a plane, facilitating interface migration, inducing less strain energy, and consequently forming smoother surfaces.[23] If multiple lattice planes were exposed during the initial nucleation stage, different growth rates of these various planes will inevitably lead to a nonuniform distribution of the electric field across the electrode surface, which would self-amplify the nonuniformity of the deposited metal, especially in an acidic environment with high exchange current densities.[24] Furthermore, for certain exposed lattice planes with sluggish diffusional kinetics, growth will preferentially occur along the 2D direction, hence preventing the formation of a uniform metal film and resulting in rough morphologies like particulates and dendrites.[25] Therefore, the growth of preferred textured lattice planes via rational selection constitutes key knowledge in making metal anodes reversible. Besides the geometric advantage of planar electrodeposition, the intrinsic inertness of these preferred textured planes to the HER should also be considered an additional benefit, because metal surfaces in corrosive aqueous acid environments can hardly form a stable solid−electrolyte interphase (SEI), hence the suppression of side reactions can only be achieved through the reduction of proton activity on the electrodeposited plane.

Here, we report the tailored electrodeposition of a textured Sn metal film in an acidic aqueous electrolyte and how it enables a highly reversible aqueous Sn battery. Given the fast nucleation rate of free Sn atoms in the acidic media, we effectively controlled the adsorption and diffusion processes of nascent Sn atoms during the deposition process by selectively adsorbing cocation species with steric hindrance, thus inhibiting the growth of competing lattice planes. The textured lattice plane is selected as preferred based on surface energy, self-diffusion barrier, and hydrogen evolution activity to ensure that this plane has the potential to grow as a film and minimizes the risk of side reactions. Preferential growth of such planes produces uniform voltage distribution on the electrode surface during deposition and unifies the growth rate across the surface, which encourages film formation over particulate or dendritic morphologies. We found that relatively dense (211)-oriented Sn film deposition is most inert toward the HER in the presence of quaternary onium cocations (e.g., tetrapentylammonium), while nonuniform, large particles would instead form with multiple planes exposed in the absence of the onium cocations. The as-deposited textured Sn film anode has high reversibility with a CE of 99.95% during cycling for over 2900 h at 5 mA cm^{-2}/5 mAh cm^{-2}, and enables stable and high areal capacity operations in various battery chemistries, i.e., MnO_2//Sn, PbO_2//Sn, and Br_2//Sn static batteries up to 7000 cycles and 10 mAh cm^{-2}. The interfacial engineering adopted in this work provides a universal strategy for regulating the electrodeposition of metals of interest.

2. RESULTS AND DISCUSSION

2.1. Acidic Metal Deposition and Aging Mechanism.

Acid-tolerant p-block Sn is one of the most promising metal materials for acidic batteries because of its high energy density, low cost, and ease of recycling.[26−28] Its intrinsic electronic structure, defined by a deeply buried d-band that is inactive in hydrogen bonding and insufficient orbital overlap between the sp-band and the hydrogen 1s orbital, gives rise to a high hydrogen adsorption free energy and correspondingly high HER overpotentials.[29] The fast deposition−dissolution process of Sn metal in acidic media also makes it a promising alternative to lead anodes, with high rate capability, low toxicity, and small environmental footprints, making it better suited for applications such as grid-scale energy storage and backup electric power storage in support of intermittent sources like solar, wave, and wind.[30] Notably, innovation efforts in cathode materials have produced exceptional candidates with high energy and fast kinetics for acidic aqueous electrolytes, but the integration of them into a full cell and subsequent commercialization have been prevented by the absence of a stable metal anode.[9,10] Although the recent development of electrodeposited Sn metal has revealed new opportunities, only a few hundred hours of cycling have been achieved with relatively low areal capacity (0.5 to 1 mAh

https://doi.org/10.1021/jacs.5c03861
J. Am. Chem. Soc. XXXX, XXX, XXX−XXX

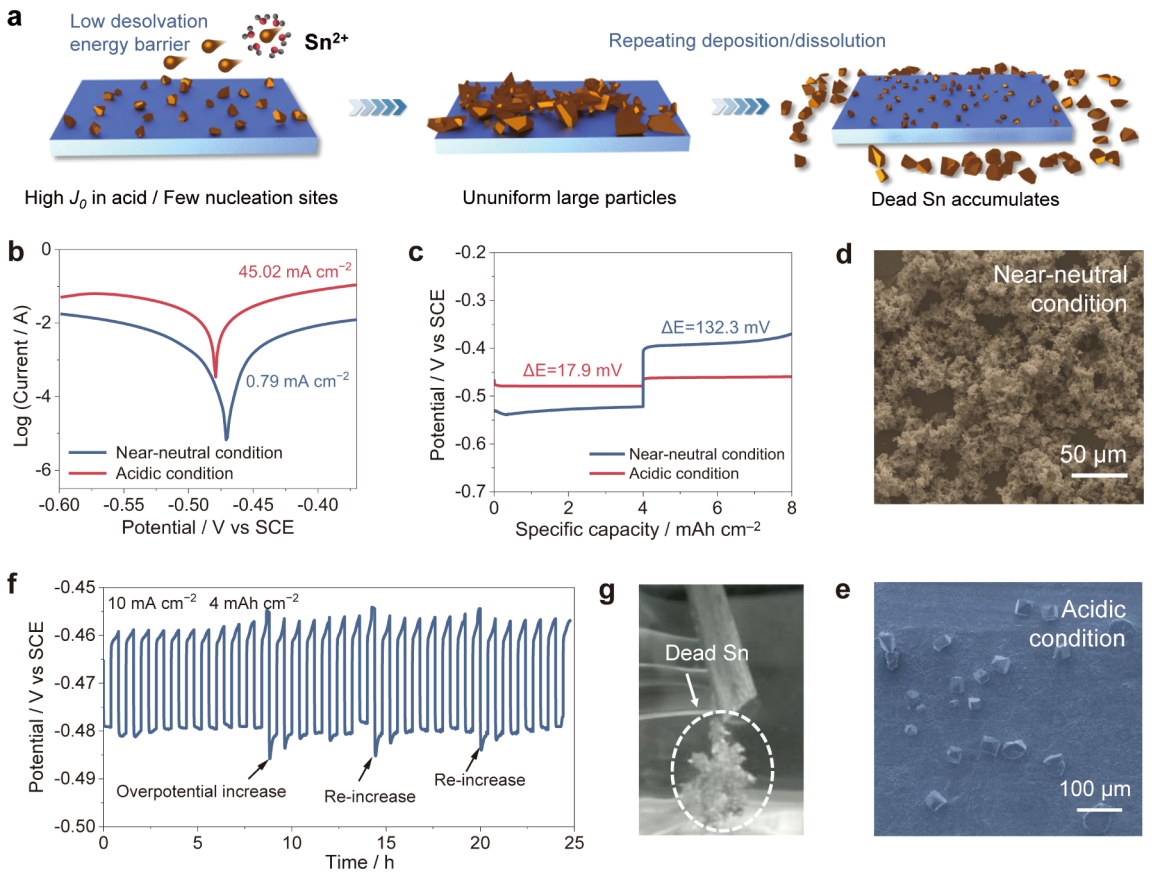

Figure 1. (a) Schematic diagram of Sn deposition from the acidic electrolyte. (b) Tafel curves and (c) polarization of the Sn electrode in near-neutral (2 M Li_2SO_4 + 0.2 M $SnSO_4$) and acidic (2 M H_2SO_4 + 0.2 M $SnSO_4$) electrolytes. SEM image of the Sn anode after Sn deposition at an areal capacity of 1 mAh cm^{-2} in the (d) near-neutral electrolyte and (e) acidic electrolyte. (f) Galvanostatic cycling stability of Sn in the acidic electrolyte at 10 mA cm^{-2} with a fixed capacity of 4 mAh cm^{-2}. (g) Optical photograph of the Sn anode in the acidic electrolyte after 31 cycles at 10 mA cm^{-2}.

cm^{-2}).[13,31−33] Making reversible Sn electrodeposition that can sustain prolonged cycling at practical areal loadings is a critical step toward commercially viable aqueous acidic batteries.

The challenge of achieving a reversible metal anode in acidic media can be reflected from its electrodeposition process. The scheme of conventional Sn metal electrodeposition displays that the large polyhedral particle morphology, caused by the intrinsic nature of acid, is the main driving force behind the irreversibility of the Sn metal anode (Figure 1a). Extracted from the Tafel polarization curves (Figure 1b), the calculated exchange current density for Sn in a conventional acidic electrolyte (2 M H_2SO_4 + 0.2 M $SnSO_4$) is ~57 times higher than that in a near-neutral electrolyte (2 M Li_2SO_4 + 0.2 M $SnSO_4$). Such high exchange current density in acid stems from the lower desolvation energy of Sn^{2+} and the fast transformation process of hydrated Sn^{2+} to free Sn atoms (Sn^0), whose electrodeposition is characterized by much lower polarization, as indicated by an overpotential of 17.9 mV compared with 132.3 mV in the near-neutral electrolyte (Figure 1c). Consequently, Sn^0 electrodeposited from the near-neutral electrolyte exhibits a morphology rich in small particulates with sizes less than 5 μm (Figure 1d), while Sn^0 deposited from an acidic electrolyte tends to promote particle growth rather than particle nucleation, leading to a uniform morphology with large particulates (Figure 1e, >20 μm).[13,32,34] The repeated electrodeposition/dissolution of Sn^0 in a three-electrode cell configuration is shown in Figure 1f. Increases of the Sn^0 nucleation overpotential are observed at the 11th, 19th, and 25th cycles, indicating that the deposited Sn^0 particles were repeatedly dislodged and became deactivated after initial deposition, thus renucleation was required at the next charge. Optical and scanning electron microscopy (SEM) images after cycling further verify that the deposition/dissolution process of nascent Sn^0 particles on the existing Sn^0 surface is irreversible in acid and consequently forms electrochemically inactive "dead Sn^0" with uneven, large-sized particles (Figure 1g and S2). Therefore, to achieve the ideal flat film morphology needed for highly reversible anodes, one must learn how to regulate and control the electrodeposition process so that the desired lattice is preferentially encouraged while other competing phases are suppressed.

2.2. Identification of the Desired Lattice Planes and Interfacial Engineering of Textured Sn^0 Deposition. Electrodeposition morphology heavily relies on voltage uniformity at the electrode interface. Different lattice planes may exhibit varying growth rates depending on the surface energy and self-diffusion barrier, while the high exchange rate between solvated metal ion M^{n+} and free metal atom M^0 in acid will enlarge such differences. The local differences in the metal particulates lead to nonuniform voltage distribution and a self-amplified particle growth pattern. Recent research results indicated that applying a neutral interfacial adsorbent could partially decrease the exchange current density, while using alloy substrates to promote the nucleation process could only

https://doi.org/10.1021/jacs.5c03861
J. Am. Chem. Soc. XXXX, XXX, XXX−XXX

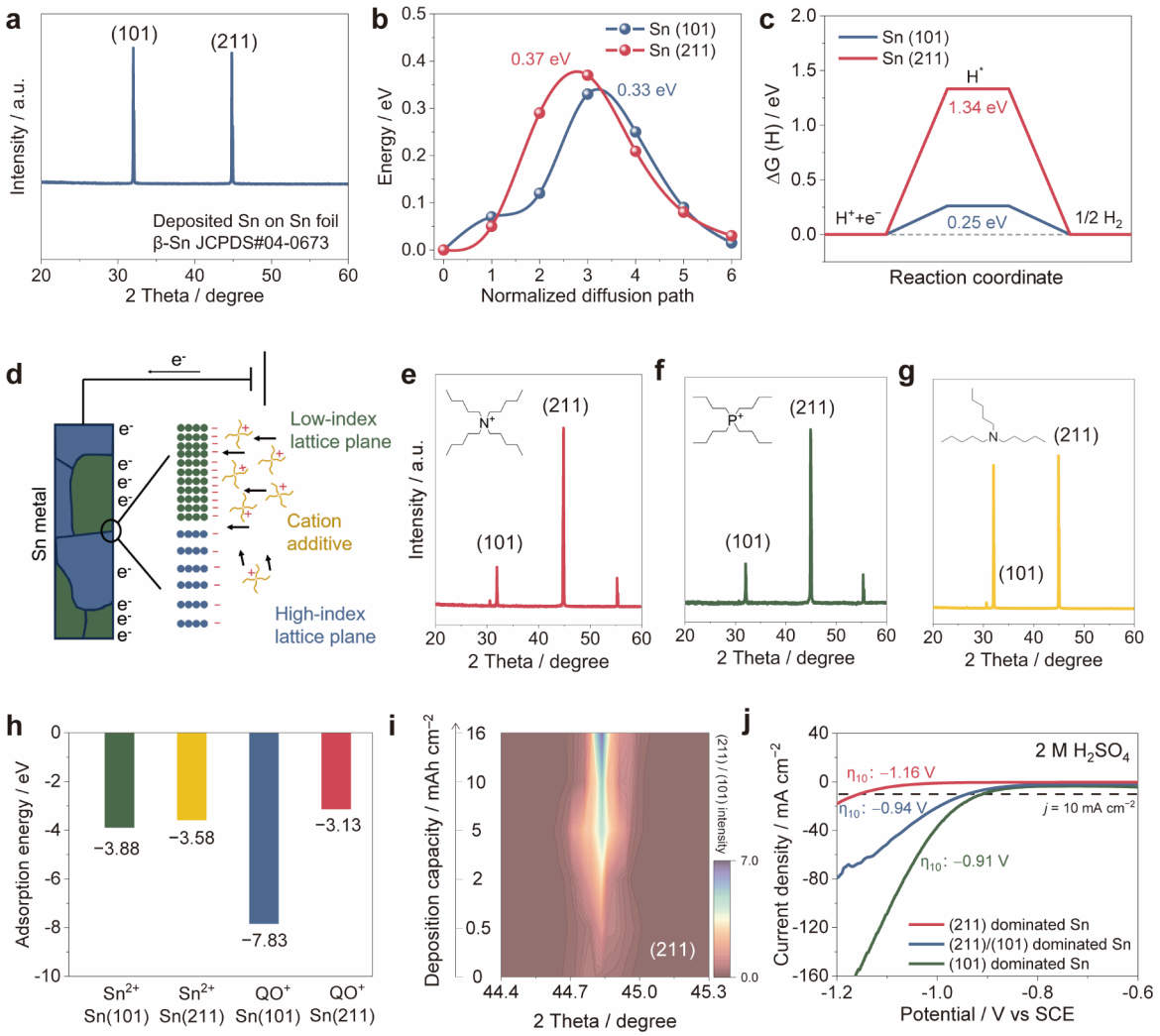

Figure 2. (a) XRD patterns of deposited Sn on a commercial Sn foil in SE at 5 mA cm^{-2} and 5 mAh cm^{-2}. (b) Self-diffusion energy barrier for Sn on (101) and (211) planes. (c) The H adsorption free energy of the active sites on Sn (101) and Sn (211). (d) The scheme of the selective adsorption principle of cocations on low-index lattice planes. XRD patterns of deposited Sn at 5 mA cm^{-2} and 5 mAh cm^{-2} with different cocation species including (e) tetrapentylammonium ion, (f) tetrabutylphosphonium ion, and (g) tripentylamine. (h) Adsorption energy simulation of QO^+ and Sn^{2+} on the Sn (101) and Sn (211) substrates. (i) The contour plot of XRD Sn (211) plane evolution along with the deposition capacity. The intensity of the (101) plane is normalized to 1. (j) LSV curves of the (211) plane-dominated Sn, (101) plane-dominated Sn, and Sn foil in 2 M H_2SO_4.

achieve more uniform Sn particle deposition of smaller size in acid, instead of the ideal planar film growth.[13,32] To intrinsically alter the electrodeposition pattern of metals in acidic media, textured growth of a specific lattice plane is carried out to minimize differences in the growth rate induced by different planes in the local environment.

The potentially exposed lattice planes of Sn metal are evaluated based on thermodynamic and kinetic parameters. The X-ray diffraction (XRD) patterns reveal that the commercial Sn foil mainly consists of (101) and (211) dominated β-Sn (JCPDS#04−0673, Figure S3). The Sn^0 particles subsequently electrodeposited on commercial Sn foil adopt the same lattices (Figure 2a) when deposited from an acidic electrolyte (2 M H_2SO_4 + 0.2 M $SnSO_4$, denoted as SE). The reported surface energy (Figure S4) and calculated self-diffusion barrier (Figure 2b and S5) for Sn (101) and Sn (211) show 7.7% and 10.3% deviations, respectively, but both parameters for the (101) plane are slightly smaller than those for the (211) plane, suggesting that both planes have the potential to be exposed during deposition, while the (101) plane experiences faster lateral growth and diffusion rates.[35] The relatively low self-diffusion barrier (<0.4 eV) could enable the possibility of textured film deposition on either plane, but the intrinsic HER overpotential on different lattice planes now becomes a determining factor because the HER is thermodynamically favorable during Sn deposition (0 V vs −0.14 V referred to SHE). Therefore, the low-index (101) plane is not ideal as the textured lattice plane because of its higher atom density, i.e., more active sites that induce the HER (Figure S6). The HER activity of the two lattice planes is also quantitatively evaluated via density functional theory (DFT) calculations (Figure 2c). The HER can be divided into two sequential steps: (1) a proton accepting an electron to form H*, and (2) H* dimerizing to become H_2.[36] Hence, the Gibbs free energy of H* (ΔG_{H^*}) is generally considered an effective descriptor to evaluate the HER activity. Compared with the (211) surface, the ΔG_{H^*} on the (101) surface shows a significantly lower absolute value (0.25 eV vs 1.34 eV),

https://doi.org/10.1021/jacs.5c03861
J. Am. Chem. Soc. XXXX, XXX, XXX−XXX

indicating a strong catalytic activity of (101) to promote the undesirable HER. Thus, prohibiting Sn^0 growth along the low-index (101) lattice plane while encouraging textured (211) electrodeposition becomes the apparent choice.

To prohibit Sn^0 deposition on a specific lattice plane, we introduce species that can create steric hindrance at interfaces by selectively adsorbing on these planes, hence blocking sustained metal deposition and suppressing the growth of this specific plane. A cation adsorbent is chosen due to the higher electron density of low-index planes. During the electrodeposition process, the metal anode is negatively polarized, which could preferentially attract a cation rather than neutral or anionic species to the low-index (101) planes (Figure 2d). As the most commonly used cocation species with adjustable steric hindrance, we select quaternary onium cations (QO^+), that is, a nitrogen- or phosphorus-centered cations substituted with four alkyl groups, for demonstration because of their low cost, chemical stability in aqueous media, and wide availability.[37] The steric hindrance of QO^+ could be easily adjusted by changing the length of the alkyl chain. For experimental verification, the crystallography of the electrodeposited Sn^0 with some QO^+ cocations was examined by X-ray diffraction (XRD). The relative texture coefficients (RTCs) are applied to illustrate the variation in preferred crystal orientation (Note S1), and a larger RTC_{hkl} value represents a higher exposure ratio of the corresponding (hkl) facets on the Sn^0 surface.[38] Figure 2e,f shows that both tetrapentylammonium (84.5% for RTC_{211}) and tetrabutylphosphonium (83.9% for RTC_{211}) cocations texturize the Sn^0 deposition toward (211) planes, significantly different from the Sn^0 deposited from the baseline electrolyte in the absence of QO^+ cocations (54.0% for RTC_{211}). Focused ion beam milling coupled with electron backscattered diffraction mapping (FIB-EBSD) was performed and revealed a preferred growth orientation close to the (211) plane in Sn^0 deposited from tetrapentylammonium cocation-added SE (Figure S7). Similar (211)-textured Sn^0 deposition is also observed under different deposition current densities (Figure S8). However, if one alkyl substituent in QO^+ is removed, rendering the additive species a neutral triamylamine molecule, no preferential growth is observed in deposited Sn^0, and the RTC_{211} value is similar to that of Sn^0 deposited from the baseline electrolyte (Figure 2g, 56.5%). These results confirm that the positive charge brought by cocation species serves as the critical factor which induces the (211)-textured Sn^0 metal deposition. Note that the four alkyl substituents in QO^+ do not need to be identical to promote the preferential Sn^0 planes, as evidenced by tributylmethylammonium cocations (Figure S9).

2.3. Theoretical and Experimental Verification of Textured Sn^0 Deposition. We set quaternary ammonium with a moderate side-chain length (i.e., tetrapentylammonium) as our model cocation in the following study, while still denoting it as QO^+ unless specifically explained. The cation-induced textural growth of Sn^0 (211) is verified by DFT simulation of adsorption energy on different lattice planes (Figure 2h and S10). The adsorption of nascent Sn^0 on Sn^0 (101) is slightly stronger compared to Sn^0 (211). However, the calculated adsorption energy of QO^+ on Sn^0 (101) is significantly lower than that on the Sn^0 (211) plane, confirming our hypothesis that QO^+ will selectively adsorb on the Sn^0 (101) plane. As a theoretical prediction, the adsorption of nascent Sn^0 on the Sn^0 (101) plane will be impeded by QO^+, which directs Sn^{2+} to deposit on the Sn^0 (211) plane due to the lower adsorption energy than that of QO^+ (−3.58 vs −3.13 eV).

The adsorption behavior of QO^+ was further studied using Raman and Fourier transform infrared (FTIR) spectra, which indicate that the QO^+ cocation does not obviously affect the solvation structure of Sn^{2+} (Figure S11). Therefore, it may mainly alter the interfacial structures on Sn^0 surfaces, where its presence regulates the electrodeposition process of Sn^0 by (dis)adsorption.[39] Alternating current (AC) voltammetry was applied to understand the adsorption behavior of QO^+ on the Sn surface.[40] The capacitance of the Sn^0 electrode in the electrolyte containing QO^+ (denoted as QO^+-SE) is slightly lower than that in the pristine electrolyte (Figure S12), which is mainly due to the thicker Faradaic double layer created by the adsorption of QO^+, whose size is much larger than Sn^{2+} and H_2O.[41] The capacitance minimum, namely the potential of zero charge, shifts negatively from 0.424 to 0.324 V (vs SCE) upon the introduction of large-volume QO^+, indicating its specific adsorption in the inner Helmholtz plane, where it partially replaces Sn^{2+} cations and reduces surface charge density.[42] This drastic change in the interfacial structure also leads to a change in open circuit voltage (Figure S13). In addition, the chemical composition of the Sn^0 anode surface after deposition was analyzed by X-ray photoelectron spectroscopy (XPS) depth profiling. Both C−N and $C-N^+$ species are present on the surface of the Sn anode in the N 1s spectra (Figure S14), suggesting that QO^+ was stably adsorbed on the Sn surface. However, the N-containing species almost disappeared when the Ar^+ sputtering depth reached 7.8 nm, indicating that QO^+ was only adsorbed on the surface and did not penetrate inside the deposited Sn^0 layer as an interfacial component. It is noteworthy that the exchange current density of Sn in QO^+-SE, calculated from Tafel slopes, is only 11.8% lower than that in the baseline electrolyte (39.69 mA cm^{-2}, Figure S15), which suggests that the presence of QO^+ does not obviously slow down the flux of working ions.

The dynamic evolution of different lattice planes of deposited Sn^0 is studied by XRD analysis. In the baseline electrolyte, the relative intensity ratio of (211)/(101) is 0.99 when Sn^0 was deposited at an areal capacity of 0.5 mAh cm^{-2}, which experiences almost no change when the deposition areal capacity goes up to 5 mAh cm^{-2}. By comparison, in the QO^+-SE electrolyte, the (211)/(101) intensity ratio was elevated from 1.57 to 4.49 as the deposition capacity increased from 0.5 mAh cm^{-2} to 5 mAh cm^{-2} (Figure S16), demonstrating that the introduction of QO^+ promotes the deposition of Sn^0 along (211) preferentially. Contour plots are also provided in Figure 2i and S17 to visualize the evolution of the (211)/(101) intensity ratio in Sn^0 deposited from the QO^+-SE electrolyte, and a gradual increase of (211) intensity was observed along with the deposition capacity. TEM reveals that both the (101) and (211) planes are observed in Sn deposited from the SE electrolyte, whereas the (211) plane prevails when Sn^0 is electrodeposited from the QO^+-SE electrolyte (Figure S18). The advantage of the (211)-textured Sn metal is further expressed in HER activity in 2 M H_2SO_4 (Figure 2j), where a delayed H_2 evolution potential was clearly detected on the (211) lattice plane-dominated Sn^0 deposited from QO^+-SE (η_{10} = −1.16 V), as compared with other Sn electrodes with a higher (101) lattice plane ratio (η_{10} = −0.94 V for (211)/(101)-dominated Sn and η_{10} = −0.91 V for (101)-dominated Sn), consistent with prior theoretical calculations (Figure 2c).

https://doi.org/10.1021/jacs.5c03861
J. Am. Chem. Soc. XXXX, XXX, XXX−XXX

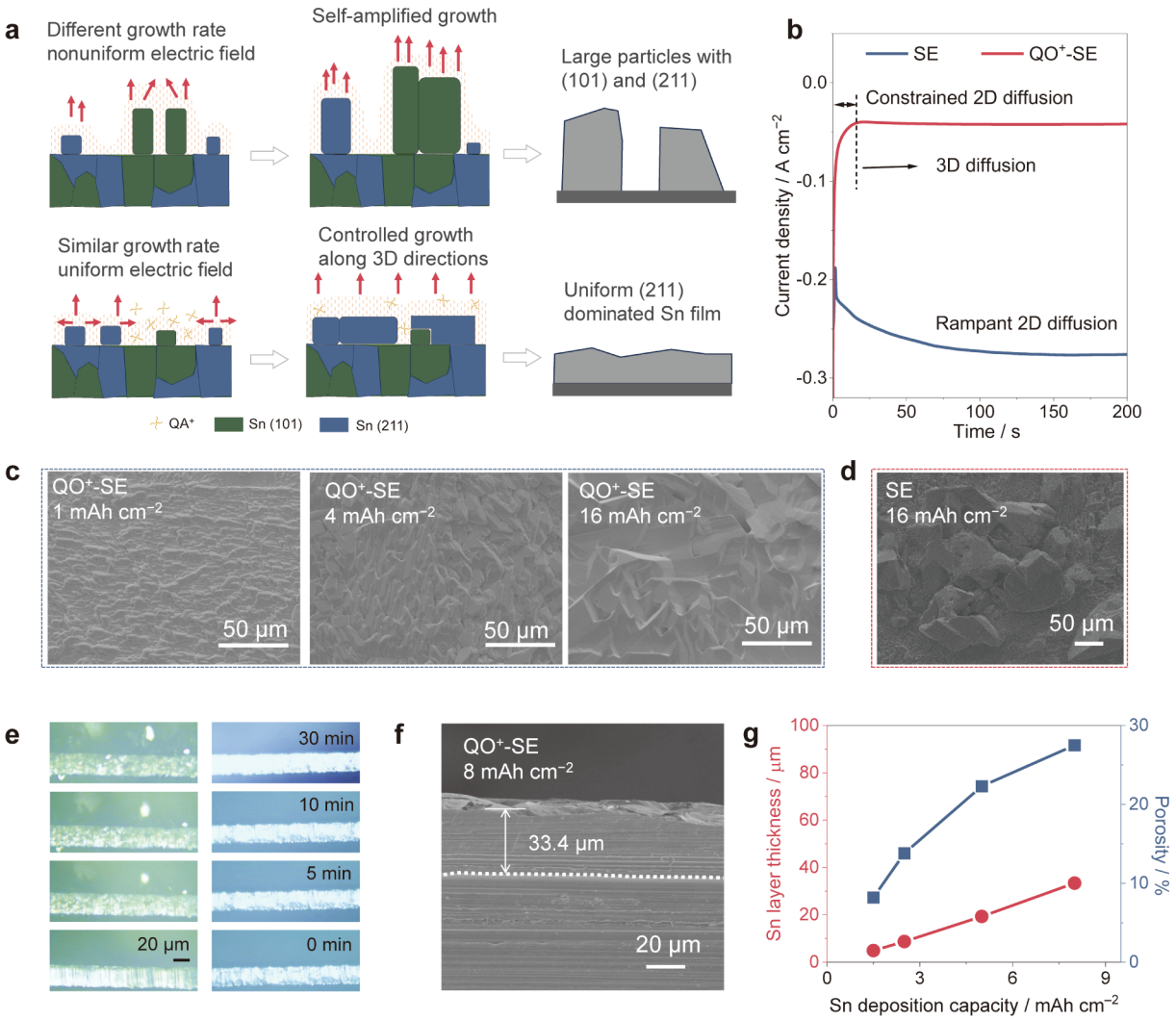

Figure 3. (a) Schematic of Sn deposition without (upper) or with (lower) QO^+ cocation. (b) CA curves of the Sn anode in SE and QO^+-SE electrolytes under −150 mV. (c) SEM images of Sn surfaces with different deposition capacities ranging from 1 mAh cm^{-2} to 16 mAh cm^{-2} in QO^+-SE. (d) SEM image of Sn surface at 16 mAh cm^{-2} in SE. (e) In-situ optical observations of Sn plating at 20 mA cm^{-2} in SE (green) and QO^+-SE (blue) electrolytes. (f) Cross-sectional SEM image of deposited Sn with a capacity of 8 mAh cm^{-2}. (g) The experimental relationship of the Sn layer thickness and porosity along with Sn deposition capacity.

2.4. Electrodeposition of the Sn^0 Film. The morphologies of electrodeposited metals are governed simultaneously by the initial nucleation and the subsequent growth rate (Figure 3a). During Sn^0 electrodeposition from conventional electrolytes, differences in growth rates for various lattice planes are amplified by an acidic environment, which is characterized by high exchange current density, which will create a local nonuniform distribution of the electric field and subsequent metal nuclei, forming "hotspots" that eventually lead to growth of satellite large particles. In contrast, the (211) plane is more inclined to favor a more uniform electric field distribution at the interface by minimizing the growth rate differences. Benefiting from the low self-diffusion energy barrier of Sn on the (211) plane (0.37 eV), the (211)-dominated Sn grains will be given the opportunity for preferential growth along all 3D directions and eventually merge together into a uniform and planar film. The relevant differences could be observed from chronoamperometry (CA) measurements of Sn^0 electrodes in SE and QO^+-SE electrolytes.[43,44] The rise in current density during the CA test is assumed to reflect an increase in the effective surface area. As shown in Figure 3b, the current density of the Sn^0 anode in the baseline electrolyte rapidly increases over 200 s, suggesting a continuous and rampant 2D nucleation process, in which the surface area of the Sn anode progressively enlarges due to the fast, nonuniform deposition of Sn^0. The Sn^{2+} ions will diffuse laterally along the surface to find the most favorable charge transfer sites, meaning that Sn^0 will aggregate on all surfaces of the nuclei and then grow into uncontrolled, large particles to minimize surface energy. This self-amplified deposition process would aggravate the formation of "dead Sn^0". Comparatively, the current density in the electrolyte with the QO^+ cocation displays a very short time (16 s) for the 2D nucleation process, followed by a constant low current density that represents a longstanding 3D compact diffusion process. The steadily decreasing current density in the first step and the constant low current in the second step indicate an entirely different Sn^0 deposition mechanism from what happens in the baseline electrolyte. This phenomenon of decreasing current emerges as a result of the reduced surface area, which is only possible when growth centers overlap and merge, yielding a dense and smooth deposit layer. The 3D compact diffusion after

https://doi.org/10.1021/jacs.5c03861
J. Am. Chem. Soc. XXXX, XXX, XXX−XXX

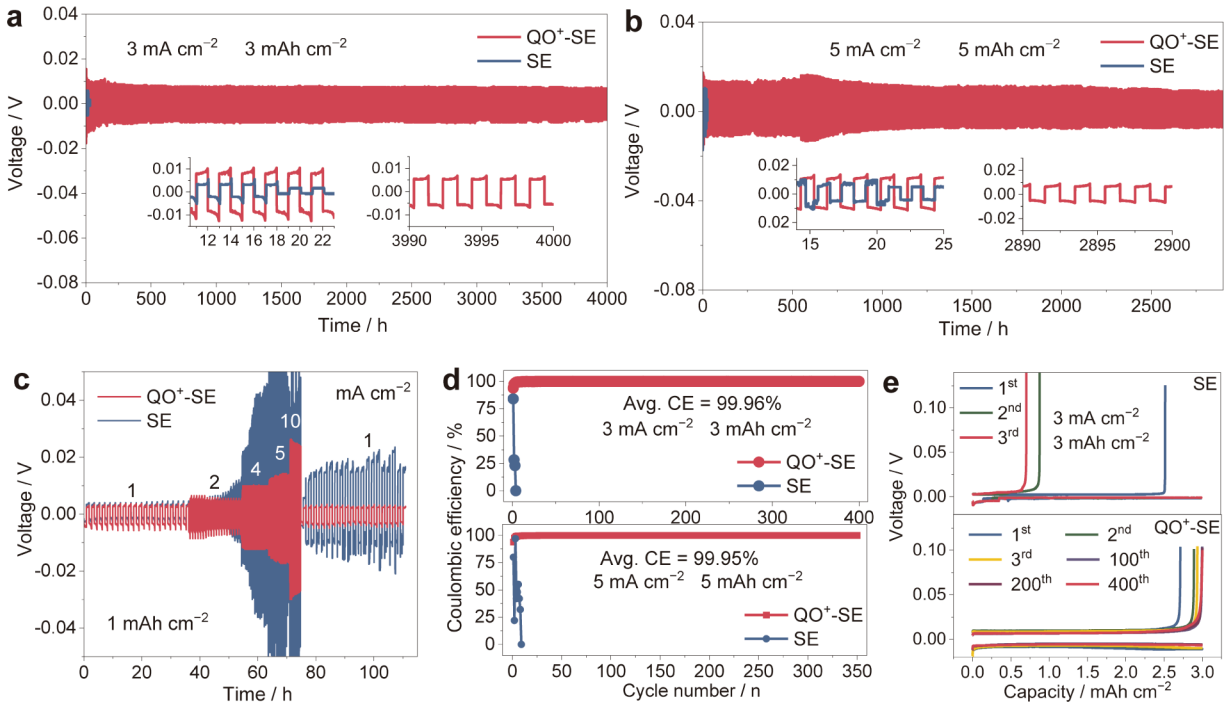

Figure 4. Long-term galvanostatic cycling of symmetric Sn cells with SE and QO^+-SE electrolytes: (a) 3 mA cm^{-2}, 3 mAh cm^{-2}, (b) 5 mA cm^{-2}, and 5 mAh cm^{-2}. (c) Rate performance of symmetric Sn cells with SE and QO^+-SE electrolytes at 1 mAh cm^{-2}. (d) CE of Sn//Cu asymmetric cells using SE and QO^+-SE electrolytes at different current densities/capacities: 3 mA cm^{-2}/3 mAh cm^{-2} (up) and 5 mA cm^{-2}/5 mAh cm^{-2} (down). (e) Voltage profiles of Sn anodes with SE (up) and QO^+-SE (down) electrolytes at 3 mA cm^{-2}/3 mAh cm^{-2}.

nucleation ensures the continuous growth of a dense Sn film layer with time without obvious surface area changes. In this unique process, Sn^{2+} is absorbed on the Sn^0 electrode surface and reduced locally with constrained 2D surface diffusion due to the additional energy barrier brought by the surface-adsorbed QO^+ on the (101) plane, which forces the absorbed Sn^{2+} to move laterally. As a result, Sn deposition in QO^+-SE becomes homogeneous without an observable volume change, which can be clearly visualized from the SEM and optical images of the Sn^0 electrode after the CA test (Figure S19). Besides, Sn^0 electrodeposited from QO^+-SE consistently exhibits a shorter 2D nucleation time and lower current density than those in the pristine electrolyte under different test potentials from −20 mV to −150 mV (Figure S20), further demonstrating that the Sn^0 deposition generated by QO^+-SE is more homogeneous.[45]

The morphologies of the electrodeposited Sn^0 metal in the presence of QO^+ are further examined by ex-situ SEM characterization as the capacities increase from 1 to 16 mAh cm^{-2} (Figure 3c). In the initial deposition step (1 mAh cm^{-2}), Sn^0 deposits in QO^+-SE display a uniform layer with a pyramidal shape on the top. Upon further increasing the Sn^0 electrodeposition capacity, the Sn^0 layer gradually merges together and forms a continuous film. By contrast, Sn deposited in the absence of QO^+ shows large, nonuniform particles with a diameter even greater than 50 μm starting at 1 mAh cm^{-2}, which continuously increase with the deposition capacity (Figure 3d and S21). These random-sized, large particles on the surface are more likely to become dead Sn^0 during the later cycling process. In-situ optical microscopy shows that Sn^0 deposited in the baseline electrolyte has rock-like protrusions after electrochemical plating for 1.67 mAh cm^{-2} (Figure 3e), but the Sn^0 from QO^+-SE still presents a flat surface throughout the plating process upto 10 mAh cm^{-2}, and no obvious protrusions are observed. The inner morphology from side-view SEM reveals a relatively dense Sn^0 film with no large pores or interparticle voids, with a total thickness growth from 4.9 to 33.4 μm as the capacity increases from 1.5 to 8 mAh cm^{-2} (Figure 3f and S22). The calculated porosity of the deposited Sn film is only 8.2% at 1.5 mAh cm^{-2}, which is relatively dense, but it will gradually increase along with the capacity (Figure 3g, 27.5% at 8 mAh cm^{-2}).

2.5. Electrochemical Reversibility of Sn^0 Anodes. The same three-electrode electrochemical test shown in Figure 1f was applied to QO^+-SE (Figure S23). As expected, the Sn^0 electrode in QO^+-SE exhibited much stable curves during cycling without the shrinkage caused by renucleation, indicating that the disconnection of deposited Sn^0 particles or formation of dead Sn^0 is successfully suppressed. The optical images of the Sn^0 electrode after the test also detect no dead Sn^0. The Sn^0//Sn^0 symmetric cells based on baseline and QO^+-SE electrolytes were assembled to validate electrodeposition reversibility. As expected, the symmetric cell cycled in the QO^+-SE electrolyte can maintain stable voltage hysteresis for over 4000 h at 3 mA cm^{-2} with a fixed capacity of 3 mAh cm^{-2}, while the symmetric cell cycled in the SE electrolyte exhibits a fluctuating voltage profile typical of side reactions and a sudden drop after 18 h, probably caused by a soft short circuit (Figure 4a). The cells cycled in the QO^+-SE electrolyte show a slightly higher polarization voltage than those in the SE electrolyte, likely due to the additional energy required to regulate the deposition of Sn^{2+} ions into the (211) plane by site-blocking onium cocations. Impressively, when cycled at practical-level capacities of 5 mAh cm^{-2} and 10 mAh cm^{-2}, the symmetric cell with the QO^+ cocation could still achieve a long lifespan of over 2900 and 300 h, respectively (Figure 4b and S24). From postcycling XRD patterns of Sn^0 anodes, we notice that the Sn^0 anode in QO^+-SE electrolyte

https://doi.org/10.1021/jacs.5c03861
J. Am. Chem. Soc. XXXX, XXX, XXX−XXX

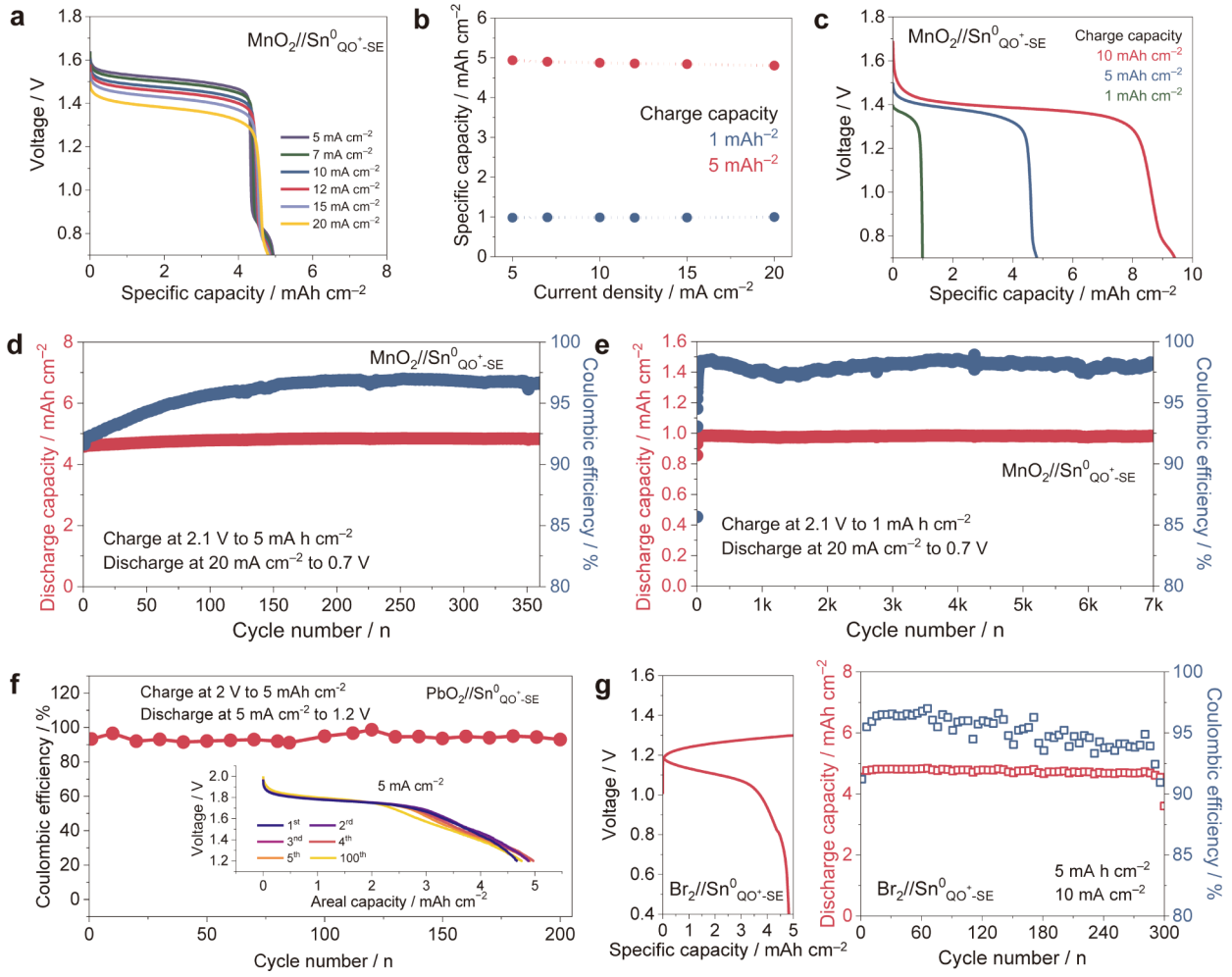

Figure 5. (a) Discharge curves with an areal capacity of 5 mAh cm^{-2} under different current densities; (b) rate performance; (c) discharge curves with different capacities from 1 to 10 mAh cm^{-2} at 20 mA cm^{-2} of the $MnO_2//Sn^0$ battery in QO^+-SE electrolytes. The cycling performance of the $MnO_2//Sn^0$ battery with the fixed deposition capacities of (d) 5 mAh cm^{-2} and (e) 1 mAh cm^{-2}. (f) The cycling performance of the $PbO_2//Sn^0$ battery with the QO^+-SE electrolyte with a fixed deposition capacity of 5 mAh cm^{-2}. (g) The charge/discharge curves and cycling performance of a $Br_2//Sn^0$ battery with a fixed deposition capacity of 5 mAh cm^{-2}.

still maintains the (211) plane-dominated feature after long cycling, showing that the growth mechanism applied by QO^+ sustains while maintaining the desired texture (Figure S25). In addition, the (101) plane formed on Sn^0 from the baseline electrolyte dominates after cycling due to its smaller surface energy and self-diffusion kinetics. However, Sn^0 (101) triggers more severe dead Sn^0 formation, which rapidly causes the failure of the cell.[46,47] The Sn^0 anode deposited from the QO^+-SE electrolyte still maintains a flat, film-like surface after long-term cycling, in stark contrast to the Sn anode with an uneven particle surface in SE.

Although introducing QO^+ into the electrolyte enables (211)-textured Sn deposition, it should be noted that the optimum concentration of QO^+ is 7.9 mM. Higher QO^+ concentrations shorten the lifespan of the Sn^0 metal anode (Figure S26), most likely due to the detrimental effects of QO^+ on the viscosity and ion transport of the electrolyte. The rate capabilities of the $Sn^0//Sn^0$ symmetric cells were also compared for the baseline electrolyte and QO^+-SE electrolytes at current densities ranging from 1 to 10 mA cm^{-2} and then back to 1 mA cm^{-2} with a fixed capacity of 1 mAh cm^{-2}. As illustrated in Figure 4c, the symmetric cell using QO^+-SE exhibited stable voltage profiles, while the baseline electrolyte caused severe voltage fluctuations. Despite the potential detrimental effects of QO^+ on viscosity and ion transport, QO^+-SE still allows the as-deposited textured Sn^0 anode to support high-rate operations at current densities of up to 5 C, showing impressive fast deposition kinetics (Figure S27).

To demonstrate the universal application of the onium cocation strategy, reversible Sn^0 electrodeposition is also demonstrated in methanesulfonic acid (MA) with higher Sn^{2+} solubility (2 M MA + 2 M $Sn(MA)_2$). In stark contrast to the failure of Sn//Sn symmetric cells within 120 h when no QO^+ is present, the cells in QO^+-SE displayed exceptional cycling stability, maintaining a consistent voltage hysteresis for over 2600 h at 3 mA/3 mAh cm^{-2}, as well as over 600 h at 5 mA/5 mAh cm^{-2}. This highlights the potential of Sn^0-based anodes in achieving a higher volumetric energy density (Figure S28). Other types of cocations selected from the QO^+ family, based on both ammonium or phosphonium cations carrying symmetric or unsymmetric alkyl substituents of varying lengths, were verified to have a similar Sn^0-stabilization function as well, which further validates the universal effectiveness of the strategy for regulating electrodeposition planes (Figure S29). The introduction of quaternary ammonium cocations with increasing side chain length leads

https://doi.org/10.1021/jacs.5c03861
J. Am. Chem. Soc. XXXX, XXX, XXX−XXX

to greater polarization in Sn//Sn symmetric cells, primarily due to enhanced steric hindrance within the inner Helmholtz layer that impedes Sn^0 deposition. Interestingly, a volcano-shaped performance trend was observed as the side chain length of the applied QO^+ cocations increased from C_1 to C_6. Short-chain cations, such as tetramethylammonium, offer limited inhibition of Sn^0 growth along the (101) plane, while excessively long chains, as in tetrahexylammonium, disrupt deposition along all planes. Additionally, longer side chains increase electrolyte viscosity, reducing ion mobility and overall performance. As a result, the tetrapentylammonium cocation provide the most favorable balance between deposition control and ion transport.

The reversibility and stability of the Sn^0 deposition/dissolution chemistry can be confirmed under more severe conditions of the "anode-free" Sn^0//Cu asymmetrical cells. At 3 mA cm^{-2}/3 mAh cm^{-2}, the Sn^0//Cu cell with the QO^+ cocation operates stably for 800 h and presents a stable average CE of 99.96% over 400 cycles, and even remains at 99.95% for 350 stable cycles after increasing the current density/capacity to 5 mA cm^{-2}/5 mAh cm^{-2} (Figure 4d). On the contrary, the anode-free Sn^0//Cu cell in the baseline electrolyte fails after only 3 cycles at 3 mA cm^{-2}/3 mAh cm^{-2}, with a fluctuating CE that rapidly drops to 0 after 8 cycles when the current density/capacity is increased to 5 mA cm^{-2}/5 mAh cm^{-2}. The corresponding plating/stripping curves are shown in Figure 4e and S30. Under the most demanding conditions, the QO^+-SE electrolyte supports the operation of an anode-free cell for hundreds of cycles at both areal capacities with stable voltage polarization and a flat plateau.

2.6. Acidic Batteries with the Textured Sn Metal Anode. Finally, to fully validate the practical use of the (211)-textured Sn film anode enabled by the QO^+ cocations, we assembled a series of full batteries constructed with various cathode materials, including MnO_2, PbO_2, and Br_2. Here, the MnO_2 cathode utilizes a dissolution/deposition mechanism in acid with a 2-electron transfer process (Figure S31).[10] The discharge curves of MnO_2//Sn^0 batteries in QO^+-SE at different current densities with a fixed charge capacity of 5 mAh cm^{-2} are depicted in Figure 5a. The as-assembled MnO_2//Sn^0 battery exhibits a flat discharge plateau of ~1.52 V at 5 mA cm^{-2}, with a maximum areal capacity of 4.94 mAh cm^{-2}. Excellent tolerance against current abuse is observed during the cycling of the MnO_2//Sn^0 battery upon the increase of the test current density, and no obvious capacity fading is detected at different charge capacities (Figure 5b and S32). Such excellent rate performance is mainly attributed to the electrochemical behavior of the electrodes, both of which experience fast dissolution and deposition of Sn^0/Sn^{2+} and MnO_2/Mn^{2+}. The rechargeable capacity of the MnO_2//Sn^0 battery can be pushed from 1 mAh cm^{-2} (98.6%) to a large areal capacity of 10 mAh cm^{-2} (94.1%), where it still maintains good CE (Figure 5c) and a maximum energy density of 130.4 Wh kg^{-1} (based on the masses of all electrodes). Impressively, the MnO_2//Sn^0 battery in the QO^+-SE electrolyte can be stably cycled over 350 cycles under a fixed capacity of 5 mAh cm^{-2} at a stable CE of 96.8% (Figure 5d). When the capacity increases to 10 mAh cm^{-2}, 60 cycles of reversible charge/discharge could still be achieved (Figure S33). If shallow cycling was conducted at 1 mAh cm^{-2}, the MnO_2//Sn^0 battery could even retain 98.2% of its theoretical capacity for over 7000 cycles (Figure 5e). No voltage drop was observed during cycling at different areal capacities (Figure S34).

An acidic aqueous battery consisting of Sn^0 as the anode and commercial cathode PbO_2 was also assembled to demonstrate the potential of Sn^0 to replace Pb^0 in popular lead-acid batteries (Figure 5f, S35, and S36). The PbO_2//Sn^0 battery with the QO^+-SE electrolyte demonstrates good cycling performance over 200 cycles at a discharge current density of 5 mA cm^{-2} and a deposition capacity of 5 mAh cm^{-2} without voltage drop, which proves that the Sn^0 is able to reversibly deliver competitive energy density while minimizing the use of toxic Pb. Furthermore, taking advantage of halogen redox chemistry, we also demonstrate a static Br_2//Sn^0 battery in HBr and QO^+-SE electrolytes (Figure 5g). An air-treated carbon felt is applied as the cathode current collector, and the detailed configuration is shown in Figure S37. Air-treated carbon felt could improve electrode hydrophilicity and catalytic activity through the introduction of oxygen-containing functional groups, thus facilitating enhanced electrolyte–electrode interactions. The voltages of the charge/discharge plateau are recorded as 1.26 and 1.10 V, with a small polarization of only 160 mV, showing high energy efficiency. The static Br_2//Sn^0 battery delivers a discharge capacity of 4.74 mAh cm^{-2} for more than 280 cycles at a fixed charge capacity of 5 mAh cm^{-2}. To compare the practical viability of various acidic aqueous batteries, Figure S38 summarizes areal capacities and discharge voltages from a few recently published works (Table S1).[13,32,48−52] It is worth noting that, while in general the cathode, active species, and cell configuration for this battery chemistry still have large space for optimization, textured Sn-based acidic aqueous batteries already stand out in this category and exhibit attractive potential for energy storage at practical-level areal capacities.

3. CONCLUSIONS

In summary, we report the identification of a desirable Sn^0 crystal plane for reversible electrodeposition, and based on this fundamental understanding, we design an onium-based cocation adsorption strategy to tailor the interfacial structure, so that the selective growth of the Sn^0 (211) plane is preferred, enabling stable and high-efficiency operation of the Sn^0 anode in acidic aqueous batteries constructed with various cathode materials. Diversified quaternary onium cations with steric hindrance were demonstrated to be effective in forming such a textured Sn^0 deposition in a uniform film. We discovered the critical issue of particle-dominated metal deposition in acids and demonstrated how to control the growth process to ensure that the particles merge into a planar metal film. Both the high hydrogen evolution overpotential and reduced contact area of the film electrode with the electrolyte contribute to the high Coulombic efficiency and reversibility. As a result, the Sn film anode optimized by the quaternary onium cocation shows a few thousand deposition/dissolution cycles with high stability under 5 mAh cm^{-2} and approaches practical-level areal capacities when coupled with different cathode materials. Our findings confirm that the reversible electrodeposited metal strongly requires the regulation of the metal growth process due to the fast kinetics of metal-ion/free atom transformation in acids. The concept of unifying the voltage distribution by texturizing metal deposition to achieve a film morphology with high reversibility can be extended to future designs for various metal anodes.

https://doi.org/10.1021/jacs.5c03861
J. Am. Chem. Soc. XXXX, XXX, XXX−XXX

■ ASSOCIATED CONTENT

Data Availability Statement

The data that support the findings of this study are available from the corresponding authors upon reasonable request.

Supporting Information

The Supporting Information is available free of charge at https://pubs.acs.org/doi/10.1021/jacs.5c03861.

Experimental section; characterization; computational methods; detailed characterization for the deposited Sn^0 structure; electrochemical evaluation for the Sn^0 anode and Sn metal batteries (PDF)

■ AUTHOR INFORMATION

Corresponding Authors

Kang Xu − *SES AI Corporation, Woburn, Massachusetts 01801, United States*; Email: kang.xu@ses.ai

Xihong Lu − *MOE of the Key Laboratory of Bioinorganic and Synthetic Chemistry, The Key Lab of Low-carbon Chem & Energy Conservation of Guangdong Province, School of Chemistry, Sun Yat-Sen University, Guangzhou 510275, China*; orcid.org/0000-0002-6764-0024; Email: luxh6@mail.sysu.edu.cn

Ying Shirley Meng − *Pritzker School of Molecular Engineering, The University of Chicago, Chicago, Illinois 60637, United States; Argonne Collaborative Center for Energy Storage Science (ACCESS), Argonne National Laboratory, Lemont, Illinois 60439, United States*; orcid.org/0000-0001-8936-8845; Email: shirleymeng@uchicago.edu

Authors

Haozhe Zhang − *Pritzker School of Molecular Engineering, The University of Chicago, Chicago, Illinois 60637, United States; Chemical Sciences and Engineering Division, Argonne National Laboratory, Lemont, Illinois 60439, United States*; orcid.org/0000-0001-6363-5271

Yanxia Yu − *MOE of the Key Laboratory of Bioinorganic and Synthetic Chemistry, The Key Lab of Low-carbon Chem & Energy Conservation of Guangdong Province, School of Chemistry, Sun Yat-Sen University, Guangzhou 510275, China*

Diyu Xu − *MOE of the Key Laboratory of Bioinorganic and Synthetic Chemistry, The Key Lab of Low-carbon Chem & Energy Conservation of Guangdong Province, School of Chemistry, Sun Yat-Sen University, Guangzhou 510275, China*

Minghao Zhang − *Pritzker School of Molecular Engineering, The University of Chicago, Chicago, Illinois 60637, United States*

Chen-Jui Huang − *Pritzker School of Molecular Engineering, The University of Chicago, Chicago, Illinois 60637, United States*; orcid.org/0000-0001-8338-1424

Jianxin Wang − *Pritzker School of Molecular Engineering, The University of Chicago, Chicago, Illinois 60637, United States; Chemical Sciences and Engineering Division, Argonne National Laboratory, Lemont, Illinois 60439, United States*; orcid.org/0009-0002-0410-5240

Hao Liu − *MOE of the Key Laboratory of Bioinorganic and Synthetic Chemistry, The Key Lab of Low-carbon Chem & Energy Conservation of Guangdong Province, School of Chemistry, Sun Yat-Sen University, Guangzhou 510275, China*

Fan Yang − *MOE of the Key Laboratory of Bioinorganic and Synthetic Chemistry, The Key Lab of Low-carbon Chem & Energy Conservation of Guangdong Province, School of Chemistry, Sun Yat-Sen University, Guangzhou 510275, China*

Mingqian Li − *Pritzker School of Molecular Engineering, The University of Chicago, Chicago, Illinois 60637, United States*

Di-Jia Liu − *Pritzker School of Molecular Engineering, The University of Chicago, Chicago, Illinois 60637, United States; Chemical Sciences and Engineering Division, Argonne National Laboratory, Lemont, Illinois 60439, United States*; orcid.org/0000-0003-1747-028X

Complete contact information is available at: https://pubs.acs.org/10.1021/jacs.5c03861

Notes

The authors declare the following competing financial interest(s): One joint patent application on this work have been filed (US US63/652925) between Polsky Center for Entrepreneurship and Innovation of the University of Chicago and Argonne National Laboratory.

■ ACKNOWLEDGMENTS

Y.S.M. acknowledges startup funding from the Pritzker School of Molecular Engineering at the University of Chicago. D.-J.L. and H.Z.Z. acknowledge the funding support from the Joint Task Force Initiative (JTFI) at the University of Chicago (2-84889-4401). Y.S.M., D.-J.L., and K.X. acknowledge the support from the Energy Transition Network at the University of Chicago. X.H.L. acknowledges the funding support from the Basic and Applied Basic Research Fund of Guangdong Province (2025A1515012868). The work performed at Argonne National Laboratory's Center for Nanoscale Materials, a U.S. Department of Energy Office of Science User Facility, was supported by the U.S. DOE, Office of Basic Energy Sciences, under Contract No. DE-AC02-06CH11357.

■ REFERENCES

(1) Zhu, Z.; Jiang, T.; Ali, M.; Meng, Y.; Jin, Y.; Cui, Y.; Chen, W. Rechargeable batteries for grid scale energy storage. *Chem. Rev.* **2022**, *122* (22), 16610−16751.

(2) Bauer, C.; Burkhardt, S.; Dasgupta, N. P.; Ellingsen, L. A.-W.; Gaines, L. L.; Hao, H.; Hischier, R.; Hu, L.; Huang, Y.; Janek, J.; et al. Charging sustainable batteries. *Nat. Sustainability* **2022**, *5* (3), 176−178.

(3) Liang, G.; Mo, F.; Ji, X.; Zhi, C. Non-metallic charge carriers for aqueous batteries. *Nat. Rev. Mater.* **2021**, *6* (2), 109−123.

(4) Liang, Y.; Yao, Y. Designing modern aqueous batteries. *Nat. Rev. Mater.* **2023**, *8* (2), 109−122.

(5) Li, M.; Lu, J.; Ji, X.; Li, Y.; Shao, Y.; Chen, Z.; Zhong, C.; Amine, K. Design strategies for nonaqueous multivalent-ion and monovalent-ion battery anodes. *Nat. Rev. Mater.* **2020**, *5* (4), 276−294.

(6) Parker, J. F.; Chervin, C. N.; Pala, I. R.; Machler, M.; Burz, M. F.; Long, J. W.; Rolison, D. R. Rechargeable nickel−3D zinc batteries: An energy-dense, safer alternative to lithium-ion. *Science* **2017**, *356* (6336), 415−418.

(7) Liang, Y.; Jing, Y.; Gheytani, S.; Lee, K.-Y.; Liu, P.; Facchetti, A.; Yao, Y. Universal quinone electrodes for long cycle life aqueous rechargeable batteries. *Nat. Mater.* **2017**, *16* (8), 841−848.

(8) Zhou, L.; Liu, L.; Hao, Z.; Yan, Z.; Yu, X.-F.; Chu, P. K.; Zhang, K.; Chen, J. Opportunities and challenges for aqueous metal-proton batteries. *Matter* **2021**, *4* (4), 1252−1273.

(9) Wu, X.; Hong, J. J.; Shin, W.; Ma, L.; Liu, T.; Bi, X.; Yuan, Y.; Qi, Y.; Surta, T. W.; Huang, W.; et al. Diffusion-free Grotthuss

topochemistry for high-rate and long-life proton batteries. *Nat. Energy* **2019**, *4* (2), 123−130.
(10) Chen, W.; Li, G.; Pei, A.; Li, Y.; Liao, L.; Wang, H.; Wan, J.; Liang, Z.; Chen, G.; Zhang, H.; et al. A manganese−hydrogen battery with potential for grid-scale energy storage. *Nat. Energy* **2018**, *3* (5), 428−435.
(11) Zheng, J.; Bock, D. C.; Tang, T.; Zhao, Q.; Yin, J.; Tallman, K. R.; Wheeler, G.; Liu, X.; Deng, Y.; Jin, S.; et al. Regulating electrodeposition morphology in high-capacity aluminium and zinc battery anodes using interfacial metal−substrate bonding. *Nat. Energy* **2021**, *6* (4), 398−406.
(12) Gilli, P.; Pretto, L.; Bertolasi, V.; Gilli, G. Predicting hydrogen-bond strengths from acid− base molecular properties. The p K a slide rule: Toward the solution of a long-lasting problem. *Acc. Chem. Res.* **2009**, *42* (1), 33−44.
(13) Yu, Z.; Wang, Q.; Li, Y.; Zhang, F.; Ma, X.; Zhang, X.; Wang, Y.; Huang, J.; Xia, Y. Highly reversible tin redox chemistry for stable anode-free acidic proton battery. *Joule* **2024**, *8* (4), 1063−1079.
(14) Liu, Y.; Xu, X.; Sadd, M.; Kapitanova, O. O.; Krivchenko, V. A.; Ban, J.; Wang, J.; Jiao, X.; Song, Z.; Song, J.; et al. Insight into the critical role of exchange current density on electrodeposition behavior of lithium metal. *Adv. Sci.* **2021**, *8* (5), 2003301.
(15) Zheng, J.; Zhao, Q.; Tang, T.; Yin, J.; Quilty, C. D.; Renderos, G. D.; Liu, X.; Deng, Y.; Wang, L.; Bock, D. C.; et al. Reversible epitaxial electrodeposition of metals in battery anodes. *Science* **2019**, *366* (6465), 645−648.
(16) Biswal, P.; Stalin, S.; Kludze, A.; Choudhury, S.; Archer, L. A. Nucleation and early stage growth of Li electrodeposits. *Nano Lett.* **2019**, *19* (11), 8191−8200.
(17) Liang, Y.; Dong, H.; Aurbach, D.; Yao, Y. Current status and future directions of multivalent metal-ion batteries. *Nat. Energy* **2020**, *5* (9), 646−656.
(18) Xu, X.; Jiao, X.; Kapitanova, O. O.; Wang, J.; Volkov, V. S.; Liu, Y.; Xiong, S. Diffusion limited current density: A watershed in electrodeposition of lithium metal anode. *Adv. Energy Mater.* **2022**, *12* (19), 2200244.
(19) Thompson, C. V.; Carel, R. Stress and grain growth in thin films. *J. Mech. Phys. Solids* **1996**, *44* (5), 657−673.
(20) Thompson, C. V.; Carel, R. Texture development in polycrystalline thin films. *Mater. Sci. Eng.* **1995**, *32* (3), 211−219.
(21) Zhang, M.; Tantratian, K.; Ham, S.-Y.; Wang, Z.; Chouchane, M.; Shimizu, R.; Bai, S.; Yang, H.; Liu, Z.; Li, L.; et al. Grain selection growth of soft metal in electrochemical processes. *Joule* **2025**, *9* (4), 101847.
(22) Wulff, G. On the question of speed of growth and dissolution of crystal surfaces. *Z. Kristallogr.* **1901**, *34* (5), 449−530.
(23) Jäckle, M.; Helmbrecht, K.; Smits, M.; Stottmeister, D.; Groß, A. Self-diffusion barriers: possible descriptors for dendrite growth in batteries? *Energy Environ. Sci.* **2018**, *11* (12), 3400−3407.
(24) Tan, J.; Ma, L.; Yi, P.; Wang, Y.; Li, Z.; Fang, Z.; Li, X.; He, S.; Wang, X.; Ye, M.; et al. Scalable Customization of Crystallographic Plane Controllable Lithium Metal Anodes for Ultralong-Lasting Lithium Metal Batteries. *Adv. Mater.* **2024**, *36* (30), 2403570.
(25) Jäckle, M.; Groß, A. Microscopic properties of lithium, sodium, and magnesium battery anode materials related to possible dendrite growth. *J. Chem. Phys.* **2014**, *141* (17), 174710.
(26) Zhang, H.; Liu, D. J.; Xu, K.; Meng, Y. S. Challenges and Opportunities for Rechargeable Aqueous Sn Metal Batteries. *Adv. Mater.* **2025**, 2417757.
(27) Zhou, W.; Song, M.; Liang, P.; Li, X.; Liu, X.; Li, H.; Zhang, T.; Wang, B.; Zhao, R.; Zhao, Z.; et al. High-Energy Sn−Ni and Sn−Air Aqueous Batteries via Stannite-Ion Electrochemistry. *J. Am. Chem. Soc.* **2023**, *145* (19), 10880−10889.
(28) Xiao, T.; Liu, L.; Liu, H.; Li, T.; Cai, D.; Lew, W. S.; Zhang, Y.; Bao, H.; Yang, J.-L.; Fan, H. J. Highly rechargeable aqueous Sn-metal-based hybrid-ion batteries. *Joule* **2025**, *9* (3), 101820.
(29) Azizi, O.; Jafarian, M.; Gobal, F.; Heli, H.; Mahjani, M. The investigation of the kinetics and mechanism of hydrogen evolution reaction on tin. *Int. J. Hydrogen Energy* **2007**, *32* (12), 1755−1761.
(30) Xu, D.; Zhang, H.; Xie, J.; Zhou, L.; Yang, F.; Ma, J.; Yu, Y.; Wang, G.; Lu, X. Highly reversible tin film anode guided via interfacial coordination effect for high energy aqueous acidic batteries. *Adv. Mater.* **2024**, *36* (35), 2408067.
(31) Li, X.; Tang, Y.; Han, C.; Wei, Z.; Fan, H.; Lv, H.; Cai, T.; Cui, Y.; Xing, W.; Yan, Z.; et al. A static tin−manganese battery with 30000-cycle lifespan based on stabilized Mn^{3+}/Mn^{2+} redox chemistry. *ACS Nano* **2023**, *17* (5), 5083−5094.
(32) Zhang, H.; Xu, D.; Yang, F.; Xie, J.; Liu, Q.; Liu, D.-J.; Zhang, M.; Lu, X.; Meng, Y. S. A high-capacity Sn metal anode for aqueous acidic batteries. *Joule* **2023**, *7* (5), 971−985.
(33) Chang, S.; Hou, W.; Del Valle-Perez, A.; Ullah, I.; Qiu, S.; Rodriguez, J. L.; Díaz-Vázquez, L. M.; Cunci, L.; Morell, G.; Wu, X. A Low-Acidity Chloride Electrolyte Enables Exceptional Reversibility and Stability in Aqueous Tin Metal Batteries. *Angew. Chem. Int. Ed.* **2025**, *64* (2), 202414346.
(34) Sahaym, U.; Miller, S. L.; Norton, M. G. Effect of plating temperature on Sn surface morphology. *Mater. Lett.* **2010**, *64* (14), 1547−1550.
(35) Tran, R.; Xu, Z.; Radhakrishnan, B.; Winston, D.; Sun, W.; Persson, K. A.; Ong, S. P. Surface energies of elemental crystals. *Sci. Data* **2016**, *3* (1), 160080.
(36) Chatenet, M.; Pollet, B. G.; Dekel, D. R.; Dionigi, F.; Deseure, J.; Millet, P.; Braatz, R. D.; Bazant, M. Z.; Eikerling, M.; Staffell, I.; et al. Water electrolysis: from textbook knowledge to the latest scientific strategies and industrial developments. *Chem. Soc. Rev.* **2022**, *51* (11), 4583−4762.
(37) Bureš, F. Quaternary ammonium compounds: simple in structure, complex in application. *Top. Curr. Chem.* **2019**, *377* (3), 14.
(38) Zhou, M.; Guo, S.; Li, J.; Luo, X.; Liu, Z.; Zhang, T.; Cao, X.; Long, M.; Lu, B.; Pan, A.; et al. Surface-preferred crystal plane for a stable and reversible zinc anode. *Adv. Mater.* **2021**, *33* (21), 2100187.
(39) Huang, C.; Zhao, X.; Liu, S.; Hao, Y.; Tang, Q.; Hu, A.; Liu, Z.; Chen, X. Stabilizing zinc anodes by regulating the electrical double layer with saccharin anions. *Adv. Mater.* **2021**, *33* (38), 2100445.
(40) Yan, C.; Li, H.-R.; Chen, X.; Zhang, X.-Q.; Cheng, X.-B.; Xu, R.; Huang, J.-Q.; Zhang, Q. Regulating the inner Helmholtz plane for stable solid electrolyte interphase on lithium metal anodes. *J. Am. Chem. Soc.* **2019**, *141* (23), 9422−9429.
(41) Shen, Z.; Mao, J.; Yu, G.; Zhang, W.; Mao, S.; Zhong, W.; Cheng, H.; Guo, J.; Zhang, J.; Lu, Y. Electrocrystallization regulation enabled stacked hexagonal platelet growth toward highly reversible zinc anodes. *Angew. Chem. Int. Ed.* **2023**, *62* (11), 202218452.
(42) Luo, J.; Xu, L.; Yang, Y.; Huang, S.; Zhou, Y.; Shao, Y.; Wang, T.; Tian, J.; Guo, S.; Zhao, J.; et al. Stable zinc anode solid electrolyte interphase via inner Helmholtz plane engineering. *Nat. Commun.* **2024**, *15* (1), 6471.
(43) Zhao, K.; Fan, G.; Liu, J.; Liu, F.; Li, J.; Zhou, X.; Ni, Y.; Yu, M.; Zhang, Y.-M.; Su, H.; et al. Boosting the kinetics and stability of Zn anodes in aqueous electrolytes with supramolecular cyclodextrin additives. *J. Am. Chem. Soc.* **2022**, *144* (25), 11129−11137.
(44) You, C.; Wu, R.; Yuan, X.; Liu, L.; Ye, J.; Fu, L.; Han, P.; Wu, Y. An inexpensive electrolyte with double-site hydrogen bonding and a regulated Zn^{2+} solvation structure for aqueous Zn-ion batteries capable of high-rate and ultra-long low-temperature operation. *Energy Environ. Sci.* **2023**, *16* (11), 5096−5107.
(45) Zhao, R.; Wang, H.; Du, H.; Yang, Y.; Gao, Z.; Qie, L.; Huang, Y. Lanthanum nitrate as aqueous electrolyte additive for favourable zinc metal electrodeposition. *Nat. Commun.* **2022**, *13* (1), 3252.
(46) Wranglén, G. Dendrites and Growth Layers in the Electro-crystallization of Metals. *Electrochim. Acta* **1960**, *2* (6), 130−143.
(47) Eckold, P.; Sellers, M.; Niewa, R.; Hügel, W. The surface energies of β-Sn—A new concept for corrosion and whisker mitigation. *Microelectron. Reliab.* **2015**, *55* (12), 2799−2807.
(48) Guo, Z.; Huang, J.; Dong, X.; Xia, Y.; Yan, L.; Wang, Z.; Wang, Y. An organic/inorganic electrode-based hydronium-ion battery. *Nat. Commun.* **2020**, *11* (1), 959.
(49) Jiang, H.; Shin, W.; Ma, L.; Hong, J. J.; Wei, Z.; Liu, Y.; Zhang, S.; Wu, X.; Xu, Y.; Guo, Q.; et al. A high-rate aqueous proton battery

https://doi.org/10.1021/jacs.5c03861
J. Am. Chem. Soc. XXXX, XXX, XXX−XXX

delivering power below− 78° C via an unfrozen phosphoric acid. *Adv. Energy Mater.* **2020**, *10* (28), 2000968.
(50) Zhu, M.; Zhao, L.; Ran, Q.; Zhang, Y.; Peng, R.; Lu, G.; Jia, X.; Chao, D.; Wang, C. Bioinspired catechol-grafting PEDOT cathode for an all-polymer aqueous proton battery with high voltage and outstanding rate capacity. *Adv. Sci.* **2022**, *9* (4), 2103896.
(51) Yue, F.; Tie, Z.; Deng, S.; Wang, S.; Yang, M.; Niu, Z. An ultralow temperature aqueous battery with proton chemistry. *Angew. Chem. Int. Ed.* **2021**, *60* (25), 13882−13886.
(52) Qiao, J.; Qin, M.; Shen, Y.-M.; Cao, J.; Chen, Z.; Xu, J. A rechargeable aqueous proton battery based on a dipyridophenazine anode and an indium hexacyanoferrate cathode. *Chem. Commun.* **2021**, *57* (35), 4307−4310.

https://doi.org/10.1021/jacs.5c03861
J. Am. Chem. Soc. XXXX, XXX, XXX−XXX